

Underwater 3D Scanner to Counteract Refraction: Calibration and Experimental Results

Miguel Castellón , Josep Forest , and Pere Ridao , *Member, IEEE*

Abstract—Underwater 3-D laser scanners are an essential type of sensors used by unmanned underwater vehicle (UUVs) for operations such as inspection, navigation, and object recognition and manipulation. This article presents a novel 3-D laser scanner, which uses a 2-axis mirror to project straight lines into the water by compensating for refraction-related distortions. This is achieved by projecting optimally curved lines, so that the refraction when they enter the water transforms them into straight lines. The relevance of this approach lies in the fact that 3-D triangulation using planes is noticeably faster than using elliptic cones. The goal of this work is twofold: first, to prove that refraction-related distortions can in practice be compensated for by using a 2-axis mirror, and second, to present a simple calibration algorithm that only needs to compute the coefficients of polynomial functions. To the best of the authors' knowledge, the prototype presented in this article is the first laser line scanner that actively counteracts the refraction of the projected light in the context of underwater robotics.

Index Terms—3-D reconstruction, 3-D sensing, autonomous underwater vehicle (AUV), underwater 3-D scanner.

NOMENCLATURE

Abbreviations

AUV	Autonomous underwater vehicle.
CMOS	Complementary metal-oxide-semiconductor.
DAC	Digital-analog converter.
DoF	Degree of freedom.
FPGA	Field-programmable gate array.
FoV	Field of view.
fps	Frames per second.
LLS	Laser line scanner.
LPF	Low-pass filter.

Manuscript received January 18, 2022; accepted April 23, 2022. Recommended by Technical Editor J. Liu and Senior Editor K. J. Kyriakopoulos. This work was supported in part by the ATLANTIS project under Grant H2020-ICT-2019-2-871571, in part by the European Commission, the PER2IAUV project under Grant PID2020-115332RB-C32, in part by the Spanish Ministry of Science, and in part by the doctoral grant of the University of Girona under Grant IFUdG2019. (*Corresponding author: Miguel Castellón.*)

The authors are with the Computer Vision and Robotics Research Institute (VICOROB), University of Girona, 17003 Girona, Spain (e-mail: miguel.castillon@udg.edu; josep.forest@udg.edu; pere@eia.udg.edu).

Color versions of one or more figures in this article are available at <https://doi.org/10.1109/TMECH.2022.3170504>.

Digital Object Identifier 10.1109/TMECH.2022.3170504

MEMS	Microelectromechanical system.
SVD	Single value decomposition.
UUV	Unmanned underwater vehicle.

I. INTRODUCTION

UNDERWATER 3-D laser line scanners (LLSs) are currently being used by unmanned underwater vehicles (UUVs) in inspection [1], object recognition [2], manipulation [3], [4], and navigation [5] tasks. This type of sensors can provide the robot with a high point cloud density at relatively fast refresh rates.

A particular type of LLSs are steered-plane scanners. These scanners typically use a rotating mirror to steer a laser plane [6], [7], which allows them to acquire 3-D information of a relatively broad field of view (FoV). This characteristic makes them suitable for manipulation tasks, in which the UUV moves at slow speeds at close distances to the target structure (around 1 m). However, this approach presents two main challenges. First, their data suffers from motion distortion when they are used to scan dynamically. A method to compensate for these distortions was proposed in [8]. Second, steering the laser plane causes it to enter the refractive surface and then the water at a nonperpendicular angle. This double refraction process deforms the original light plane into an elliptic cone [9]. Performing 3-D triangulation using elliptic cones is noticeably more computationally expensive than using planes [9]. In order to be able to project light planes in the water with a steered-plane LLS, a theoretical projection model was introduced in a previous work [10]. This model proved that using a 2-axis mirror enabled the projection of optimally curved surfaces that become planes when entering water (or, more accurately speaking, cones with a negligible curvature).

This article presents the hardware realization of that theoretical model into a prototype (see Fig. 1), whose working principle is schematically shown in Fig. 2. Thanks to the calibration process, an optimally curved scanning pattern can be computed, which when going through the flat viewport is transformed into straight lines due to refraction. The laser module is a point source. However, the trigger of the camera is synchronized with the mirror so that it opens at the beginning of each line and closes at the end of it. This means that for the camera the scanning pattern is actually made up of lines.

This article has the following two main goals: 1) to prove that refraction-related distortions can in practice be compensated for by using a 2-axis mirror; and 2) to present a simple calibration

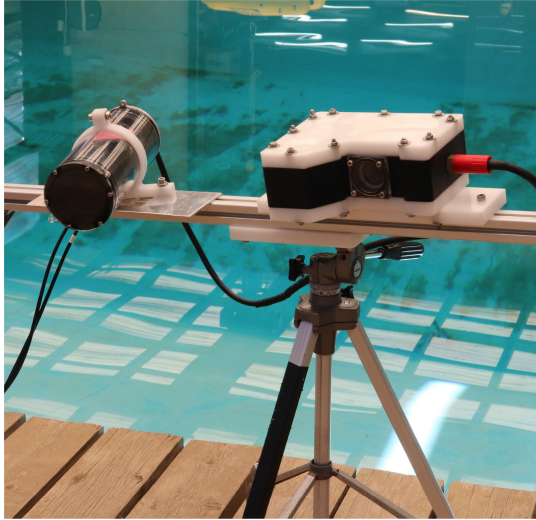


Fig. 1. Prototype of the underwater 3-D scanner. All its components are sealed together in the waterproof casing, except for the camera, which is placed in the waterproof cylinder.

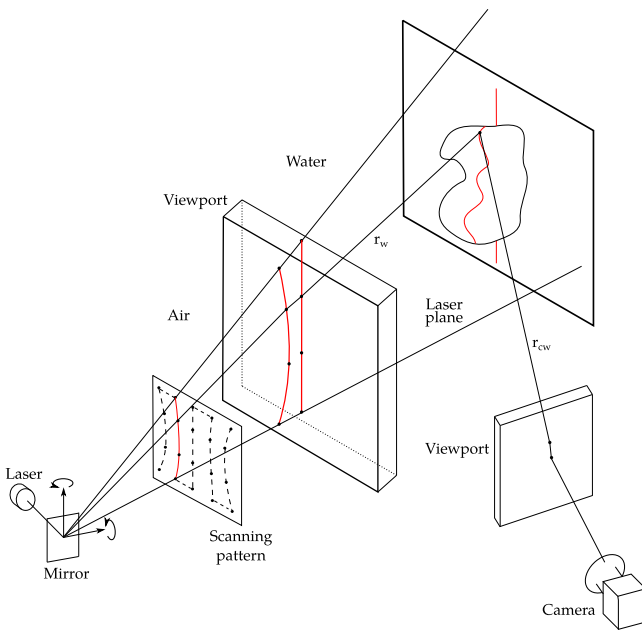


Fig. 2. Working principle of the scanner. The 2-axis mirror steers the laser beam following a set of pre-computed waypoints that form an optimally-curved set of lines, so that they become straight vertical lines when they enter the water.

algorithm that only needs to compute the coefficients of polynomial functions. These goals may be considered fulfilled if the results of 3-D triangulation using planes are accurate enough. In the context of 3-D sensing in autonomous underwater missions, a good enough accuracy should be in the order of millimeters.

A thorough review of the working principles and performance characteristics of state-of-the-art underwater 3-D laser scanners was presented in [11, Sec. 5]. However, comparing the performance of different underwater scanners in the literature is not a trivial task, since the authors report different performance

TABLE I
ACCURACY COMPARISON OF UNDERWATER TRIANGULATION SCANNERS IN THE LITERATURE

Authors	Accuracy [mm]	Range [m]
Chi [6]	1.0	1.0
Constantinou [12]	10	0.7
Lopes [13]	0.22	0.44
Massot [14]	3.6	0.7
Matos [15]	0.48	0.29
Palomer [7]	0.98	1.0
Risholm [16]	0.4	0.8
Sarafraz [17]	2.3	1.5

parameters measured in different ways. The results of this study have been summarized here in Table I for triangulation-based scanners. Broadly speaking, they all report accuracies in the order of millimeters at ranges of around 1 m. The scanning range is important, because the resolution of triangulation-based scanners worsens for increasing distances to the object [11]. As previously stated, the main goal of the presented scanner is to counteract refraction while keeping an accuracy of the 3-D reconstruction in the order of millimeters, like other systems in the literature.

The rest of this article is structured as follows. First, an overview of the system is done in Section II. Then, a new calibration algorithm based on simple projection functions is proposed in Section III. The experimental results of scanning under water are analyzed in Section IV. Finally, Section V concludes this article.

II. SENSOR DESCRIPTION

This section provides with an overview of the presented prototype. First, its theoretical projection model is explained in Section II-A. Then, a detailed explanation of its working principle is presented in Section II-B. Finally, the performance characteristics of the hardware components used in the prototype are gathered in Section II-C. Throughout the whole explanation, all the geometric variables are assumed referred to the camera reference frame $\{C\}$.

A. Sensor Model

The working principle of the proposed scanner is conceptually shown in Fig. 2 and it consists basically on two main steps: light projection and light sensing. Regarding the light projection part, the laser ray first comes out of the laser source and is reflected by the 2-axis mirror, which is driven to visit the sequence of precomputed waypoints in the scanning pattern. Then, the light passes through a wide-angle lens, which amplifies the incoming angle in order to increase the scanner FoV (not drawn in the figure for the sake of clarity). Later, the laser beam suffers a double refraction process due to the different refraction indices of the subsequent media (air, glass, and water), according to Snell's Law [18]. Finally, the laser beam hits the target to be scanned and bounces back toward the camera through the camera viewport, where the double refraction happens in reverse order (water to glass, and then glass to air). This last step constitutes the light sensing part.

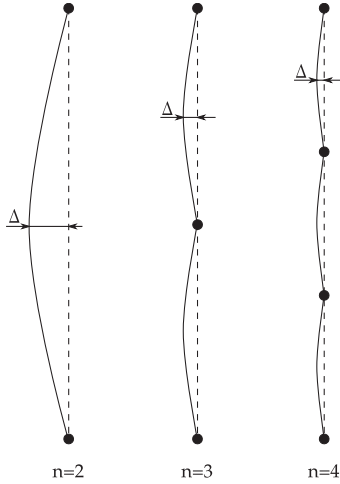


Fig. 5. Maximum deviation Δ of the actual light trajectory between waypoints with respect to the ideal one. An increasing number of waypoints per lines results in a smaller deviation.

discrete waypoints in the pattern are optimally placed to counteract refraction. Nonetheless, the mirror follows the shortest path between waypoints in angle space, which causes a deviation (see Fig. 5). On the other hand, a higher number of waypoints per line also results in a slower scanning speed (see Section IV-C).

- 3) Compute the voltage pair needed to project each point using (5) and (6)

$$\begin{aligned} V_{ijx} &= f_5(p_{ijx}, p_{ijy}) \\ V_{ijy} &= f_6(p_{ijx}, p_{ijy}). \end{aligned} \quad (11)$$

- 4) Fit a plane to the set of points corresponding to the same line. Since all the points corresponding to the same line are colinear, an intermediate step is required. For each waypoint \mathbf{p}_{ij} , another waypoint \mathbf{p}_{ij}^+ can be defined in the direction of its corresponding direction vector \mathbf{v}_{wij}

$$\mathbf{p}_{ij}^+ = \mathbf{p}_{ij} + \lambda \mathbf{v}_{wij} \quad (12)$$

where the unit direction vector is computed using (3) and (4)

$$\mathbf{v}_{wij} = \begin{bmatrix} f_3(V_{ijx}, V_{ijy}) \\ f_4(V_{ijx}, V_{ijy}) \\ \sqrt{1 - v_{ijx}^2 - v_{ijy}^2} \end{bmatrix}. \quad (13)$$

This way, the extended set of waypoints corresponding to the i th line \mathcal{P}_i can be defined as made up of all the corresponding \mathbf{p}_{ij} and \mathbf{p}_{ij}^+ . This set can now be used to compute the best-fitting plane

$$\pi_{Li} = \text{fit_plane}(\mathcal{P}_i) \quad (14)$$

where the `fit_plane` function is based on the single value decomposition (SVD) of the 3-D coordinates of the points in \mathcal{P}_i [19].

- 5) Finally, the 3-D position of each reconstructed scanned point is computed as the intersection of the camera ray

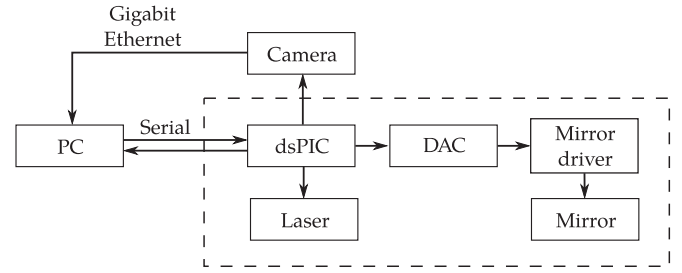


Fig. 6. Connections between the different hardware components of the proposed scanner.

with the corresponding light plane

$$S = \pi_{Li} \cap \mathbf{r}_{cw}. \quad (15)$$

The direction of the camera ray \mathbf{r}_{cw} can be computed in the reference frame of the camera $\{C\}$ as the line that passes through the camera focal point and the pixel (u, v) at which the laser line is detected:

$$\mathbf{r}_{cw} = \mathbf{0} + \lambda \begin{bmatrix} u - c_x & v - c_y & 1 \end{bmatrix}^T \quad (16)$$

where $[c_x, c_y]$ is the camera center and $[f_x, f_y]$ is the focal length.

C. Hardware

The scanner prototype is divided in two sealed water-proof boxes with transparent viewports, as shown in Fig. 1. The cylinder seals the camera, whereas the box encloses the laser module, the MEMS mirror, the wide-angle lens, and all the electronic components. The scheme of electronic connections between the different components is depicted in Fig. 6. Basically, the central computer communicates with all the elements by programming a dsPIC microcontroller, which synchronizes the rotations of the mirror with the trigger of the camera. In order to pass the required voltages to the mirror actuators, the signal coming out of the processing goes first through the digital-analog converter and then to the analog driver of the mirror. The camera transfers the information of the scanned laser line directly to the computer through a gigabit Ethernet connection. The PC may also be integrated as an on-board computer, so that the UUV can dive freely. The performance characteristics of the different components are now reviewed.

The camera used in the scanner is a CMOS sensor equipped with an FPGA for fast laser line detection. At full resolution (2048×1088 pixels) it can work in laser-detection mode at a rate of 339 fps. A lens with a focal length of 8 mm is mounted on the sensor.

The laser module projects a laser beam of 60 mW of output power at a wavelength of 520 nm. The beam diameter at the aperture is of 1 mm and the beam divergence is of 1.1 mrad.

The wide-angle lens used to increase the FoV of the scanner has an approximately linear behavior: it increases the angle of the incoming light ray by a factor of roughly 3.

The mirror has a circular reflective surface with a diameter of 1.2 mm and maximum mechanical tilting angles of approximately $\pm 5^\circ$ in each axis. The output angle achieved by the mirror actuators is only linear with respect to the input voltage for small angles. As the input voltage gets closer to the maximum voltage, severe nonlinearities appear.

The dynamic behavior of each of both of its axes can in principle be approximated to a second-order system [20] with resonance frequency of 1.3 kHz and a damping ratio $\xi = 6.5 \times 10^{-3}$. This means that it is a highly resonant system and that even small changes in the input voltages cause large overshoots in its tilting angles. In order to limit these overshoots, an LPF is applied to the input voltage signal that avoids exciting the resonance frequency. The downside of this approach is that it limits the speed of the scanner, as reported in Section IV-C. Nonetheless, it is already enough for typical autonomous object manipulation missions. An option to increase its speed would be substituting the LPF by an inverse plant filter [21], which can reportedly drive the mirror 2 orders of magnitude faster without overshooting. Yet another option could be controlling the tilting angles in closed loop [22]. However, this last approach would need to have feedback of the actual tilting angles, which is unavailable in the current configuration.

III. CALIBRATION

This section explains in detail the procedure to calibrate the projection functions of the laser scanner in order to enable the 3-D reconstruction. In brief, this method follows three subsequent steps: first, the camera intrinsic parameters are calibrated in air according to the pinhole model, along with the distortion parameters (see Section III-A). Second, the parameters of the camera viewport are calibrated in water (see Section III-B). Finally, the coefficients of the numeric projection functions are calibrated (also in water, see Section III-C). The first two steps correspond to the application of already presented methods. The third one, however, has been designed for this prototype with the aim of reducing the complexity of the calibration algorithm. Consequently, the discussion in Section III-C is noticeably longer than Sections III-A and III-B.

A. Camera Intrinsic Parameters (in Air)

The first step consists in calibrating the intrinsic parameters of the camera: the camera center $[c_x, c_y]$ and the focal lengths $[f_x, f_y]$, as well as its radial and tangential distortion coefficients. This can be done following a standard, well-known calibration routine, such as the one implemented in the OpenCV library [23]. This step is necessary for the triangulation process [see (15) and (16)].

B. Camera Viewport (in Water)

In this step, the parameters to be calibrated are the 6-DoF pose of the camera viewport with respect to the camera, the thicknesses of the camera viewport and the refraction indices of the water and of the viewport material, respectively. The index of refraction of air is used as reference ($\eta_{\text{air}} = 1$).

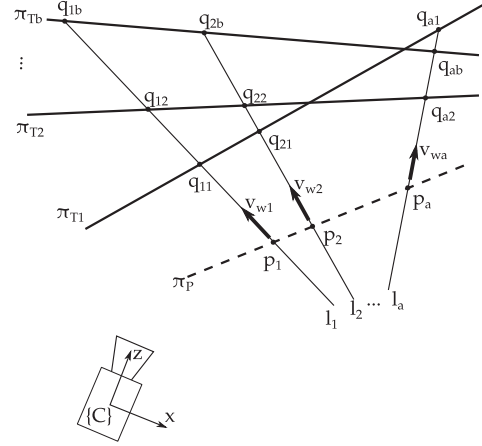


Fig. 7. In-air calibration data gathering.

The procedure basically consists in gathering an underwater dataset made up of images of a calibration pattern. Then, an optimization algorithm finds the viewport parameters by minimizing the reprojection error. The interested reader can find in [7, Sec. VI-C], a detailed explanation of the algorithm.

C. Projection Functions (in Water)

The last part of the calibration process is estimating the coefficients of the projection functions. The steps of this procedure are explained in detail in this section.

1) *Dataset Gathering*: First, a set of a voltage pairs is defined

$$\mathbf{V} = [\mathbf{V}_1 \dots \mathbf{V}_a]^T. \quad (17)$$

This set of voltages is usually chosen as an equidistant pattern covering the whole FoV of the scanner in both axes. The scanner is first placed looking at a calibration plane π_{T1} at an arbitrary position (see Fig. 7). This calibration plane has some fiducial markers attached to it. The ground-truth position of the plane with respect to the camera is computed by applying the Perspective-n-Point algorithm to those known fiducial markers. The camera grabs an image of the projected laser dot for each voltage pair in \mathbf{V} that is applied to the 2-axis mirror. This is repeated for b different positions of the calibration plane, resulting in a total of $a \times b$ images.

For each one of these images, the pixel position of the laser dot on the image plane (u, v) is found by means of the circle Hough transform [24]. The camera ray is computed by substituting the values of (u, v) in (16). The intersection of the camera ray corresponding to voltage \mathbf{V}_k with the calibration plane π_{T1} defines the 3-D position of the point \mathbf{q}_{kl} . This way, a dataset is built that contains $a \times b$ 3-D points.

2) *Voltage Line Fitting*: The next step is fitting a line to the 3-D points corresponding to the same voltage pair. For the voltage pair \mathbf{V}_k , the best-fitting line \mathbf{l}_k is defined as

$$\mathbf{l}_k \equiv \mathbf{p}_k + \lambda \mathbf{v}_{wk}. \quad (18)$$

This way, there is a set of a 3-D points \mathbf{p}_k with their corresponding unit direction vectors \mathbf{v}_{wk} . The line-fitting algorithm

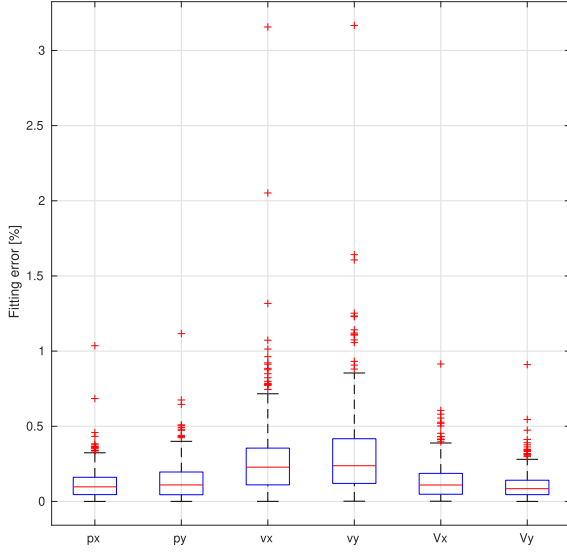


Fig. 8. Percent fitting error of the projection functions to real calibration data for functions f_1 to f_6 .

is based on SVD applied to the set of corresponding 3-D points [19].

3) *Function Coefficients*: The coefficients of all the functions in (1) to (6) are found by minimizing the following residuals:

$$\beta_1^* = \arg \min \sum_{k=1}^a \|p_{kx} - f_1(V_{kx}, V_{ky}, \beta_1)\|^2 \quad (19)$$

$$\beta_2^* = \arg \min \sum_{k=1}^a \|p_{ky} - f_2(V_{kx}, V_{ky}, \beta_2)\|^2 \quad (20)$$

$$\beta_3^* = \arg \min \sum_{k=1}^a \|v_{wkx} - f_3(V_{kx}, V_{ky}, \beta_3)\|^2 \quad (21)$$

$$\beta_4^* = \arg \min \sum_{k=1}^a \|v_{wky} - f_4(V_{kx}, V_{ky}, \beta_4)\|^2 \quad (22)$$

$$\beta_5^* = \arg \min \sum_{k=1}^a \|V_{kx} - f_5(p_{kx}, p_{ky}, \beta_5)\|^2 \quad (23)$$

$$\beta_6^* = \arg \min \sum_{k=1}^a \|V_{ky} - f_6(p_{kx}, p_{ky}, \beta_6)\|^2 \quad (24)$$

where β_i is the vector containing the coefficients of function f_i . It was experimentally chosen that all the functions f_1 to f_6 were fifth-order polynomials. In order to validate this choice, the fitting error to real calibration data is shown in Fig. 8. It can be seen in the figure that the vast majority of data points have a fitting error well below 1%. This proves that this choice of projection functions is suitable to actual data. All the minimization algorithms are implemented in C++ with the Ceres solver [25].

IV. EXPERIMENTAL RESULTS

This sections presents and discusses the numerical results of three sets of experiments. The first two of these sets are aimed at

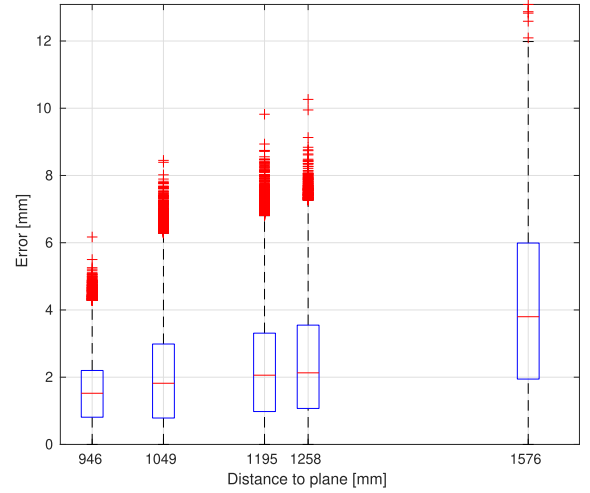


Fig. 9. Boxplot of plane fitting error.

studying the accuracy of the underwater 3-D laser scanner. On the one hand, a calibration plane with very high planarity was scanned to analyze the depth accuracy of the 3-D reconstruction at different scan ranges (see Section IV-A). On the other hand, the lateral accuracy of the scanner was assessed by scanning a calibration sphere of known radius (see Section IV-B). The goal of the third set of experiments was to study the effect of the number of waypoints per line in two important performance characteristics: accuracy and scanning speed (see Section IV-C).

All the data were gathered in the water tank of CIRS lab. The scanner was mounted on a tripod and submerged at a depth of around 1 m in clear water. In all the cases studied here, both the scanner and the scanned object (plane or sphere) were static. The standard scanning pattern used was made up of 500 lines with 50 waypoints per line (25 k waypoints in total). The FoV of the scanner is of approximately $35^\circ \times 35^\circ$. However, not the whole FoV was used in all the experiments.

With the current configuration of baseline of approximately 0.6 m between laser box and camera, the scanning range is roughly between 0.5 m and 3 m. However, most of the presented results were taken at a range between 1 m and 1.5 m, which is the most relevant for object manipulation. Measurements at shorter ranges are expected to have greater accuracy (see Fig. 13, with range of 0.6 m), whereas longer distances are typically out of the manipulation range of UUVs.

As a side note, it is worth mentioning that the apparently large number of outliers present in several of the boxplots is only due to the much larger amount of data points. The maximum outlier ratio is 0.7%.

A. Plane Fitting Error

In this set of experiments, a calibration plane was scanned at five different positions. The resulting data is shown in the boxplot of Fig. 9. The error measure is the distance of each point to the fitted plane. Additionally, the spatial distribution of the plane fitting error is plotted in Fig. 10.

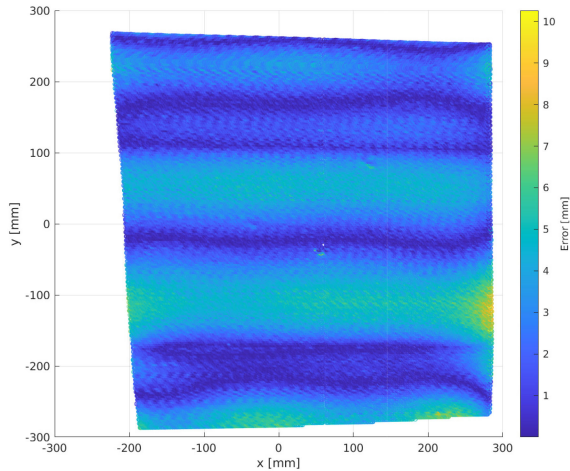


Fig. 10. Spatial distribution of the plane fitting error at an average distance of 1257.7 mm.

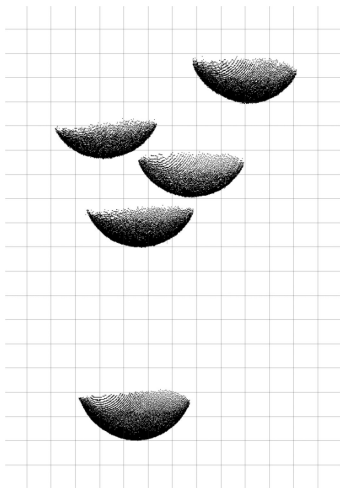


Fig. 11. Top view of the reconstructed point clouds of the calibration sphere at five different positions. The size of the blue grid is 20 mm \times 20 mm.

Two main conclusions can be drawn from these charts. On the one hand, the resulting error is in the order of a few millimeters, which is a satisfactory for the typical object manipulation tasks performed by UUVs. On the other hand, it can be seen that the error increases for an increasing scanning range. This is an expected result of a triangulation-based 3-D scanner, as explained in [11]. The accuracy level is in the order of what has been reported for other systems in the literature (see Table I).

B. Sphere Fitting Error

In this set of experiments, the scanned object was a calibration sphere with a radius of 100 mm. The reconstructed point clouds are shown in Fig. 11. The sphere fitting error of those resulting point clouds along with the radius error of the least-squares fitted sphere are shown in Fig. 12. Similarly to the previous section, the magnitude of the errors are in the order of a few millimeters. In this case, the errors are distributed between the radius error and the fitting error. Consequently, establishing the relationship between error and scan range is not as simple as with the plane.

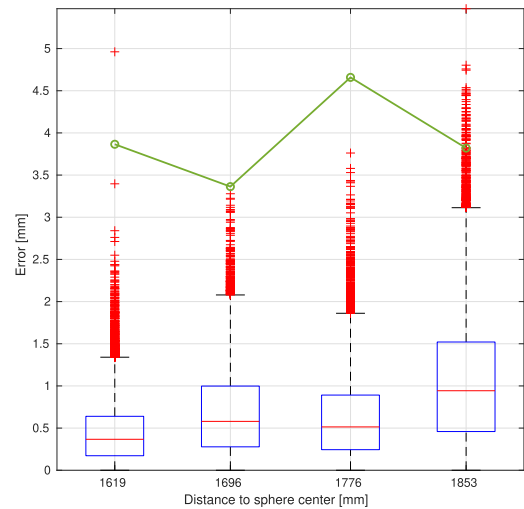


Fig. 12. Boxplot of sphere fitting error. The green line shows the radius error for a ground-truth radius of 100 mm.

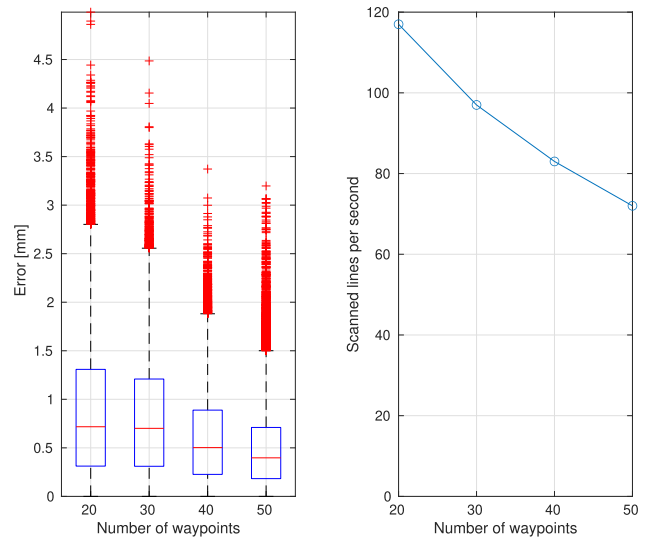


Fig. 13. Boxplot in the left shows the plane fitting residual for scan patterns with increasing number of waypoints per line. Similarly, the plot in the right shows the number of scanned lines per second for scan patterns with increasing number of waypoints per line.

C. Accuracy and Speed Versus Number of Waypoints Per Line

As mentioned in Section II-B, the choice on the number of waypoints per line in the pattern has an effect on the accuracy and speed of the 3-D reconstruction. In order to study this tradeoff in practice, scanning patterns with different number of waypoints per line were used to scan the calibration plane. The position of the plane was kept constant throughout the experiment at an approximate distance of 0.6 m. The results are shown in Fig. 13. As studied in [10], a higher number of waypoints per line means a higher accuracy. However, due to the dynamic behavior** of the mirror, it also results in a slower scanning speed. Despite having room for improvement, a scanning speed of roughly 70 lines per second is equivalent to 140 k points/s, which is already enough for a dense reconstruction of the object to be manipulated.

V. CONCLUSION

A novel 3-D underwater laser scanner has been presented that can actively counteract refraction-related distortions caused by a flat refractive surface in the projection of light. The low 3-D reconstruction errors reported in this work prove that the scanner can be used by UUVs to perform object manipulation tasks satisfactorily.

In reference to the goals of the work presented in the abstract, it has been experimentally proved that refraction-related distortion can be compensated for by using a biaxial 2-axis mirror. This has been reliably indicated by the low 3-D reconstruction errors of the different scanned objects, namely planes and spheres. Throughout the whole reconstruction process (including the calibration), it has always been assumed that the scanner can project planes in the water. Low 3-D reconstruction errors using planes consequently validate this assumption. For the same reason, the simple calibration based on numeric projection functions has been proved suitable. Therefore, and in spite of the practical limitations of the current system, we believe that the approach presented in this work can open the door to other interesting lines of research, such as optimal scanning patterns and refraction counteraction strategies.

The future steps in this line of research will be to use this 3-D underwater laser scanner mounted on an UUV in object manipulation tasks in realistic scenarios. Despite the fact that the current scanning speed is enough for typical manipulation tasks, it would be beneficial to investigate how to increase it. The most plausible strategy would be a more sophisticated dynamic control of the mirror actuators, such as the one presented in [21]. A different possible upgrade would be using a laser source with higher output power. This would probably enable 3-D reconstruction in more challenging light conditions. Finally, it will also be interesting to study the effect of varying water refraction index on the accuracy of the output point cloud. This step will be fundamental for operations in sea water.

REFERENCES

- [1] A. Palomer, P. Ridao, and D. Ribas, "Inspection of an underwater structure using point cloud SLAM with an AUV and a laser scanner," *J. Field Robot.*, vol. 36, no. 8, pp. 1333–1344, 2019.
- [2] K. Himri, P. Ridao, and N. Gracias, "Underwater object recognition using point-features, bayesian estimation and semantic information," *Sensors*, vol. 21, no. 5, pp. 1–27, Mar. 2021. [Online]. Available: <https://www.mdpi.com/1424-8220/21/5/1807>
- [3] A. Palomer, P. Ridao, D. Youakim, D. Ribas, J. Forest, and Y. Petillot, "3D laser scanner for underwater manipulation," *Sensors*, vol. 18, no. 4, pp. 1–14, 2018.
- [4] R. Pi, P. Cieslak, P. Ridao, and P. J. Sanz, "TWINBOT: Autonomous underwater cooperative transportation," *IEEE Access*, vol. 9, pp. 37668–37684, 2021. [Online]. Available: <https://ieeexplore.ieee.org/document/9367135/>
- [5] F. R. Dalglish, S. Tetlow, and R. L. Allwood, "Experiments in laser-assisted visual sensing for AUV navigation," *Control Eng. Pract.*, vol. 12, no. 12, pp. 1561–1573, 2004. [Online]. Available: https://ac.els-cdn.com/S0967066103002594/1-s2.0-S0967066103002594-main.pdf?_tid=7d62f36a-e123-4310-a955-cff1e6446ed1&acdnat=1548408210_461d9c24e11c75c9fce5244ac192b6e6
- [6] S. Chi, Z. Xie, and W. Chen, "A laser line auto-scanning system for underwater 3D reconstruction," *Sensors*, vol. 16, no. 9, Sep. 2016, Art. no. 1534. [Online]. Available: <http://www.mdpi.com/1424-8220/16/9/1534>
- [7] A. Palomer, P. Ridao, J. Forest, and D. Ribas, "Underwater laser scanner: Ray-based model and calibration," *IEEE/ASME Trans. Mechatron.*, vol. 24, no. 5, pp. 1986–1997, Oct. 2019.
- [8] M. Castellón, R. Pi, N. Palomeras, and P. Ridao, "Extrinsic visual-inertial calibration for motion distortion correction of underwater 3D scans," *IEEE Access*, vol. 9, pp. 93384–93398, 2021. [Online]. Available: <https://ieeexplore.ieee.org/document/9464334/>
- [9] A. Palomer, P. Ridao, D. Ribas, and J. Forest, "Underwater 3D laser scanners: The deformation of the plane," in *Lecture Notes in Control and Inf. Sci.*, vol. 474. Cham, Switzerland: Springer, 2017, pp. 73–88. [Online]. Available: http://link.springer.com/10.1007/978-3-319-55372-6_4
- [10] M. Castellón, A. Palomer, J. Forest, and P. Ridao, "Underwater 3D scanner model using a biaxial MEMS mirror," *IEEE Access*, vol. 9, pp. 50231–50243, 2021. [Online]. Available: <https://ieeexplore.ieee.org/document/9388657/>
- [11] M. Castellón, A. Palomer, J. Forest, and P. Ridao, "State of the art of underwater active optical 3D scanners," *Sensors*, vol. 19, no. 23, 2019, Art. no. 5161. [Online]. Available: <https://www.mdpi.com/1424-8220/19/23/5161>
- [12] C. C. Constantinou, S. G. Loizou, and G. P. Georgiades, "An underwater laser vision system for relative 3-D posture estimation to mesh-like targets," in *Proc. IEEE Int. Conf. Intell. Robots Syst.*, 2016, pp. 2036–2041. [Online]. Available: <https://ieeexplore.ieee.org/document/7759320/>
- [13] F. Lopes, H. Silva, J. M. Almeida, A. Martins, and E. Silva, "Structured light system for underwater inspection operations," in *Proc. IEEE/MTS OCEANS Genova: Discovering Sustain. Ocean Energy for a New World*, 2015, pp. 1–6. [Online]. Available: <https://ieeexplore.ieee.org/document/7271564/>
- [14] M. Massot-Campos and G. Oliver-Codina, "Underwater laser-based structured light system for one-shot 3D reconstruction," in *Proc. IEEE Sensors*, 2014, pp. 1138–1141. [Online]. Available: <https://ieeexplore.ieee.org/lpdocs/epic03/wrapper.htm?arnumber=6985208>
- [15] G. Matos, P. D. Buschinelli, and T. Pinto, "Underwater laser triangulation sensor model with flat refractive interfaces," *IEEE J. Ocean. Eng.*, vol. 45, no. 3, pp. 937–945, Jul. 2020. [Online]. Available: <https://ieeexplore.ieee.org/document/8644043/>
- [16] P. Risholm, T. Kirkhus, and J. T. Thielemann, "High-resolution structured light 3D sensor for autonomous underwater inspection," in *Proc. IEEE/MTS OCEANS Conf.*, Charleston, SC, USA, 2018, pp. 1–5. [Online]. Available: <https://ieeexplore.ieee.org/document/8604930/>
- [17] A. Sarafraz and B. K. Haus, "A structured light method for underwater surface reconstruction," *ISPRS J. Photogramm. Remote Sens.*, vol. 114, pp. 40–52, Apr. 2016. [Online]. Available: <https://www.sciencedirect.com/science/article/pii/S0924271616000290>
- [18] E. Hecht, Optics. 5th ed. London, U.K.: Pearson Education Limited, 2017. [Online]. Available: www.pearsoneditions.com
- [19] I. Söderkvist, "Using SVD for some fitting problems," no. 2, pp. 2–5, 2009. [Online]. Available: https://www.ltu.se/cms_fs/1.51590/svd-fitting.pdf
- [20] G. F. Franklin, J. D. Powell, M. L. Workman, and A. A. > Others, *Digital Control of Dynamic Systems*, vol. 3. Reading, MA, USA: Addison-Wesley, 1998.
- [21] V. Milanović, K. Castelino, and S. P. Ave, "Sub-100 μ s settling time and low voltage operation for gimbal-less two-axis scanners," in *IEEE/LEOS Opt. MEMS*, Takamatsu, Japan, vol. 15, no. 2, pp. 2003–2004, Aug. 2004. [Online]. Available: http://www.adriaticresearch.org/Research/pdf/VM_MOEMS04.pdf
- [22] V. Milanović, A. Kasturi, J. Yang, and F. Hu, "Closed-loop control of gimbal-less MEMS mirrors for increased bandwidth in LiDAR applications," in *Proc. Laser Radar Technol. Appl.*, 2017, Art. no. 101910N. [Online]. Available: www.mirrorcletech.com
- [23] OpenCV, "Tutorial: Camera calibration with OpenCV," Accessed: May 4, 2022. [Online]. Available: https://docs.opencv.org/4.x/d4/d94/tutorial_camera_calibration.html
- [24] J. Illingworth and J. Kittler, "The adaptive hough transform," *IEEE Trans. Pattern Anal. Mach. Intell.*, vol. PAMI-9, no. 5, pp. 690–698, Sep. 1987.
- [25] S. Agarwal, K. Mierle, and The Ceres Solver Team, "Ceres solver," Mar. 2022. [Online]. Available: <https://github.com/ceres-solver/ceres-solver>



Miguel Castellón received the B.Sc. degree in industrial engineering from the University of Zaragoza, Zaragoza, Spain, in 2015 and the M.Sc. degree in mechanical engineering from KU Leuven, Leuven, Belgium, in 2018. He is currently working toward the Ph.D. degree in robotics with the University of Girona, Girona, Spain.

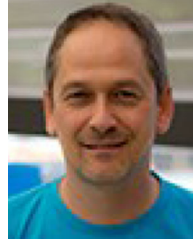
His research interests include computer vision applied to robotics and autonomous navigation.



Josep Forest received the B.Sc. degree in industrial informatics from the University of Girona, Girona, Spain, in 1992, the M.Sc. degree in electronics engineering from the Autonomous University of Barcelona, Bellaterra, Spain, in 1998, and the Ph.D. degree in industrial engineering from the University of Girona, in 2004.

He is a former Co-Founder of AQSENSE (now part of COGNEX) and OPSIS Vision Technologies Spin-Off companies. His research interests

are focused on 3D-machine vision, including laser triangulation, calibration, detection and point cloud processing. His research also includes the usability of 3-D applied to the industry for dimensional testing and quality control applications.



Pere Ridao (Member, IEEE) received the Ph.D. degree in industrial engineering from the University of Girona, Girona, Spain, in 2001.

He was the Chair of the IFAC's Technical Committee on Marine Systems. He is currently the Director of the Computer Vision and Robotics Research Institute (VICOROB) and the head of the Underwater Robotics Research Center (CIRS), and an Associate Professor with the Department of Computer Engineering, University of Girona. He is the Co-Author of four

licenses and one Spanish/European patent, being co-founder of Iqua Robotics S.L. spin-off company. Since 1997, he has participated in 24 research projects (15 European and 9 National), he is also the author of more than 100 publications, and he has directed nine Ph.D. thesis (4 more under direction) and 14 M.S. thesis. His research activity focuses on designing and developing autonomous underwater vehicles for 3-D mapping and intervention.